

# Frictional Stability of Porous Tuff Breccia Under Subsurface Pressure Conditions and Implications for Shallow Seismicity

Kazuo Mizoguchi (✉ [k-mizo@criepi.denken.or.jp](mailto:k-mizo@criepi.denken.or.jp))

Central Research Institute of Electric Power Industry <https://orcid.org/0000-0003-3340-2965>

Shin-ichi Uehara

Toho University: Toho Daigaku

Takehiro Hirose

Japan Agency for Marine-Earth Science and Technology: Kaiyo Kenkyu Kaihatsu Kiko

Sachiko Iizuka

Ceres Inc.

---

## Full paper

**Keywords:** tuff breccia, frictional strength, velocity dependent friction, shallow seismicity, sediment cover, earthquake dynamics

**Posted Date:** January 4th, 2021

**DOI:** <https://doi.org/10.21203/rs.3.rs-137406/v1>

**License:**  This work is licensed under a Creative Commons Attribution 4.0 International License.

[Read Full License](#)

---

- 1   **Title page:**
- 2   **Title: Frictional stability of porous tuff breccia under subsurface**
- 3   **pressure conditions and implications for shallow seismicity      Version**
- 4   **20181221**
- 5   Author #1: Kazuo Mizoguchi, Central Research Institute of Electric Power Industry,
- 6   1646 Abiko, Abiko, Chiba, 270-1194, Japan, [k-mizo@criepi.denken.or.jp](mailto:k-mizo@criepi.denken.or.jp)
- 7   Author #2: Shin-ichi Uehara, Graduate School of Science, Toho University, 2-2-1
- 8   Miyama, Funabashi, Chiba, 274-8510, Japan, [shinichi.uehara@sci.toho-u.ac.jp](mailto:shinichi.uehara@sci.toho-u.ac.jp)
- 9   Author #3: Takehiro Hirose, Kochi Institute for Core Sample Research, Japan Agency  
for Marine-Earth Science and Technology, 200 Monobe Otsu, Nankoku, Kochi, 783-
- 10   8502, Japan, [hiroset@jamstec.go.jp](mailto:hiroset@jamstec.go.jp)
- 11   Author #4: Sachiko Iizuka, CERES Inc., 1646 Abiko, Abiko, Chiba, 270-1194, Japan, s-
- 12   *iizuka@ceresco.jp*
- 13
- 14
- 15   **Corresponding author: Kazuo Mizoguchi**
- 16

17    **Abstract**

18    Thick layers of unconsolidated sediments are widespread in the Japan island's surface,  
19    and their frictional properties significantly affect the shallow slip behavior during  
20    earthquakes. However, laboratory data on the properties of the shallow zone remain  
21    limited. We collected tuff breccia samples from deep borehole cores of the Miocene  
22    “Green Tuff” formation, a major surface cover, and performed velocity-stepping  
23    friction tests on them under in situ stresses of 2 to 20 MPa to assess the velocity-  
24    dependence of frictional strength. The samples exhibit predominantly frictionally stable,  
25    velocity-strengthening behavior over the range of normal stress tested, which supports  
26    the hypothesis that shallow sediment layers are seismically quiescent. The result is  
27    consistent with the low seismicity and attenuation of coseismic slip in the shallow zone  
28    observed for the regional earthquakes. Microstructural observations of the postmortem  
29    samples through optical and scanning electron microscopies indicate a fabric transition  
30    from boundary shear localization to distributed cataclastic flow with increasing normal  
31    stress. Our laboratory investigation on depth-variable distribution of friction velocity  
32    dependence of a shallow sediment layer would provide further insight into the

33 mechanical role for earthquake rupture dynamics and shallow seismicity.

34

35 **Keywords**

36 tuff breccia, frictional strength, velocity dependent friction, shallow seismicity,

37 sediment cover, earthquake dynamics

38

39 **Introduction**

40 Seismological observations have shown that microearthquake activity is largely

41 concentrated in the upper portion of brittle crust, named the seismogenic layer. The

42 thickness of this layer varies from 10 km to 50 km, strongly dependent on the thermal

43 structure in different tectonic settings and is a critical index to estimate the depth extent

44 of fault rupture area and its proportional seismic moment release (magnitude) of

45 potential future earthquakes (e.g., Ito 1999; Maggi et al. 2000; Nazareth and Hauksson,

46 2004). From the point of view of rock deformation mechanism, the bottom of the

47 seismogenic layer is considered to correspond to a transition from frictional/brittle

48 regime to plastic regime, as temperature increases with depth (Sibson 1982, 1983;

49      Fredrich et al. 1989). Following the introduction and development of a rate- and state-  
50      dependent friction law, where the sign of response of friction to transient  
51      increase/decrease of sliding velocity are included as a critical benchmark of earthquake  
52      instability (Dieterich 1979; Ruina 1983), it is suggested that the lower boundary is  
53      consistent with the transition from unstable velocity-weakening (negative) field to  
54      stable velocity-strengthening (positive) field (Tse and Rice 1986; Blanpied et al. 1991).  
55      Meanwhile, above the seismogenic layer, there is a seismically quiescent zone of  
56      several kilometers thick in the subsurface (Doser and Kanamori 1986; Marone and  
57      Scholz 1988).

58      The presence of the shallow zone has been shown to significantly influence fault  
59      behaviors during dynamic earthquake rupture and its resultant properties of strong  
60      ground motion (Marone et al. 1991; Brune and Anooshehpoor 1998; Scholz 1998; Day  
61      and Ely 2002). For large earthquakes, a fault slip is likely to nucleate near the base of  
62      the seismogenic layer (Sibson 1982, 1983; Das and Scholz 1983), and then propagate  
63      upward as well as downward along faults. Detailed studies on coseismic slip  
64      distribution determined from slip inversions of geodetic data has indicated that when

65 entering into the shallow zone, further upward migration of the rupture tends to be  
66 evidently hindered, resulting in a decrease in coseismic slip with proximity to the  
67 ground surface (Wald and Heaton 1994; Simons et al. 2002; Fialko et al. 2005). Over  
68 the last decades, the cause of such shallow slip deficit has been discussed, especially in  
69 relation to frictional properties of shallow zone materials (Marone et al. 1991; Scholz  
70 1998; Fialko et al. 2005; Zinke et al. 2014). It is found that earthquake cycle simulation  
71 involving depth variation in velocity-dependent friction model including the shallow  
72 velocity-strengthening regime can reproduce the decrease in on-fault slip toward the  
73 surface (Marone et al. 1991; Rice 1993). Aside from the frictional properties of the fault  
74 plane, another explanation on the shallow slip deficit is that disperse off-fault  
75 deformation of protolith medium during coseismic as well as interseismic periods can  
76 accommodate some part of expected elastic strain energy comparable to that at deep  
77 depths because of low rigidity and velocity-strengthening property of the medium under  
78 shallow conditions (Fialko et al. 2005; Kaneko and Fialko 2011). When the rupture is  
79 confined to the shallow zone without breaching the surface, the near-field ground  
80 motion is amplified (Somerville 2003; Pitarka et al. 2009), thereby imposing more

81 severe damage to infrastructures in inland earthquake source areas. For subduction zone  
82 earthquake, whether the suppression of rupture propagation in the shallow part occurs or  
83 not is directly linked to the generation of devastating tsunami (Hyndman et al. 1997;  
84 Moore et al. 2007; Fujiwara et al. 2011; Ito et al. 2011; Kodaira et al. 2012). For  
85 instances, several experimental studies have reported frictional properties on the  
86 samples retrieved from the shallow part of the Japan trench subduction zone in order to  
87 investigate why during the 2011 Tohoku-Oki earthquake the rupture accompanying an  
88 extraordinary large slip has passed the shallow part, traditionally thought to be  
89 frictionally stable, and reached the sea floor to generate huge tsunamis (Ujiie et al.  
90 2013; Ikari et al. 2015; Sawai et al. 2017). Our knowledge of frictional properties of  
91 crustal shallow zone is essential for understanding of earthquake rupture process and  
92 further improvement of seismic hazard assessment, but it remains incomplete owing to  
93 the paucity of laboratory data except for major continental faults and plate boundary  
94 faults (Verberne et al. 2010; Carpenter et al. 2011; Boulton et al. 2012; Carpenter et al.  
95 2015; Ikari et al. 2015; Niemeijer et al. 2016).  
96 For the Japan island arc, where intraplate crustal earthquakes frequently occur

97 (Matsuda 1977; Wesnousky et al. 1984), greater than 50 % of the surface are dominated  
98 by Quaternary and Neogene unconsolidated clastic and volcaniclastic km-scale thick  
99 sediments that fill the fore-arc and back-arc basins and the volcanic front region and  
100 overlie crystalline or metamorphic basement rocks (von Huene et al. 1982; Murata and  
101 Kano 1995). In this study, we aim at investigating the rate-dependence of frictional  
102 resistance of a thick sediment layer overlying basement rocks, widely covering the  
103 inland earthquake source area, using velocity-stepping friction tests in a bi-axial shear  
104 configuration, under pressure conditions of up to ~ 2 km depth. The friction tests were  
105 conducted on porous tuff breccia samples collected from 60 m depth of a borehole  
106 drilled in the Miocene “Green Tuff” formation, a thick deposit over the Japan Sea side  
107 of Northeast Japan (Huzioka 1963; Kikuchi et al. 1991). We analyzed the experimental  
108 data with the Dieterich’s rate and state friction law (Dieterich 1979, 1981),  
109 demonstrating the variation in friction parameters as a function of normal stress. In  
110 addition, microstructural observations on the deformed samples allowed us to discuss  
111 the relationship between the variable friction behavior and the deformation mechanism.  
112 The laboratory-derived shallow zone properties we present here enable more rigorous

113 discussion on the impact of the unconsolidated shallow zone on slip behavior during an  
114 earthquake.

115

## 116 **Experimental procedures**

### 117 **Samples**

118 The samples used in this study were taken from porous andesitic tuff breccia of the  
119 Anamizu (Iwaine) Formation on the shore of the Noto Peninsula in central Japan  
120 (Figure 1). The pyroclastic rock is a member of the “Green Tuff” Formation, comprising  
121 several thousand meters of thick sequences of volcaniclastic deposits from submarine  
122 volcanism associated with the opening of the Japan Sea during late Oligocene to middle  
123 Miocene (Kikuchi et al. 1991; Sato and Amano 1991; Kano et al. 2007). These deposits  
124 are distributed over an area of 44,000 km<sup>2</sup>, corresponding to more than 10 % of the  
125 island, along the Japan Sea coast (Huzioka 1963; Murata and Kano 1995). The “Green  
126 tuff” area has experienced three large earthquakes in the last two decades including the  
127 2004 M6.6 mid-Niigata prefecture earthquake, the 2007 M6.6 Niigataken Chuetsu-oki  
128 earthquake, and the 2007 M6.7 Noto Hanto earthquake, from the database of the Japan

129 Meteorological Agency (JMA).

130 Stratigraphic studies have shown that the Anamizu Formation which the

131 experimental samples belong to is ~ 2 km thick at the Noto region (Kaseno 1965; Ozaki

132 et al. 2010). For the friction experiment, fresh core samples of the tuff breccia retrieved

133 from the Miocene Anamizu Formation at a depth of 60 m following drilling in the

134 middle western coast of the Peninsula (Figure 1) were utilized. With optical microscopic

135 observation combined with powder X-ray diffraction analysis (Figure 2a and 2b), we

136 confirmed that the tuff breccia sample is composed of phenocrysts of plagioclase,

137 orthopyroxene, and clinopyroxene with average size of ~ 1 mm in a fine-grained

138 groundmass of plagioclase, clinopyroxene and glass, with alteration products of

139 smectite and hematite. The porosity of the rock, estimated by measuring the weight

140 difference between completely dried and water-saturated ones under atmospheric

141 conditions, ranges between 19.5% and 26.1%. In addition, the bulk density, which is the

142 mass divided by the volume including any pore space is calculated to be  $2030 \pm 80$

143  $\text{kg/m}^3$ .

144

145     **Bi-axial double direct shear loading apparatus**

146     For the friction tests in this study, we utilized a newly installed **Bi-Axial double**

147     direct **S**Hear loading apparatus (**BASH**), designed at the Central Research Institute of

148     Electric Power Industry and manufactured by Marui Co., Ltd (Japan). The three main

149     components of the apparatus include: shear loading unit with a maximum load of 1000

150     kN, a stroke of 50 mm, and sliding velocities ranging from 0.1  $\mu\text{m/s}$  to 5 mm/s; a

151     specimen chamber unit with 500 mm in length, 300 mm in height, and 100 mm in

152     width; and a normal load unit with a maximum load of 600 kN (Figure 3a).

153     In the shear loading unit, a rotary shaft is connected between a 22 kW servo-

154     controlled electric motor with a maximum rotation speed of 1500 rpm and an optionally

155     attached 1/4 reduction gear and a 1000 kN ball screw jack, via a gear system for

156     adjusting the rotation speed (Figure 3a). The gear system provides a direct line and two

157     speed-down output lines with ratios of 1/11 and 1/29, respectively. The rotation from the

158     motor is converted by the screw jack to linear motion of the horizontal shaft, exerting a

159     shear load on the facing rock sample in the chamber. The three speed lines are engaged

160     manually using the combination of an electromagnetic tooth clutch and three single-disc

161 electromagnetic clutches to produce the target sliding velocity of the horizontal shaft. A  
162 load cell (SLC in Figure 3a) with a capacity of 1000 kN and a resolution of 5 kN for  
163 shear force and a strain gauge-type displacement transducer (SDT in Figure 3a) with a  
164 capacity of 100 mm and a resolution of 0.1 mm for sliding distance are positioned on  
165 the shear loading shaft. For the low stress experiments performed in this study, we  
166 temporarily installed a 100 kN load cell with a 0.05 kN resolution and an 80 mm laser  
167 displacement sensor with a 0.25  $\mu\text{m}$  resolution on the shaft.

168 The sample chamber can host three rock samples with contact areas of  $50 \text{ cm} \times 10$   
169 cm and 10 cm thickness. The central block is sandwiched between the side blocks and  
170 pressed by the horizontally moving shaft connected to the screw jack in the double-  
171 direct shear configuration (Figure 3a). When conducting the single-direct shear friction  
172 experiment, the lower stationary rock block is replaced by a stainless-steel block with  
173 the similar dimensions involving a low-friction roller at the bottom (Figure 3b). For  
174 small rock samples with dimensions of  $10 \text{ cm} \times 5 \text{ cm}$  such as used in the present study,  
175 the extra assembly shown in Figure 3c is installed into the chamber.  
176 The normal load unit comprises three 200 kN hydraulic cylinders, with each

177 containing a 660 mL air accumulator for oil pressure less than 45 MPa, a 17.6 mL  
178 spring-charged accumulator for higher pressure, and a manual screw hydraulic pump for  
179 stabilizing the oil pressure fluctuation caused by a fault-normal dilatancy/compaction of  
180  $\leq$ 5 mm during shear experiments. A 70 MPa hydraulic motor-driven pump supplies  
181 pressurized oil to the cylinders. The hydraulic cylinders are aligned parallel to the shear  
182 direction at an interval of 17 cm, with the oil pressure in each cylinder controlled  
183 independently. This allows the application of a normal load on 50 cm long rock sample  
184 in spatially uniform or non-uniform manner. A load cell (NLC in Figure 3a) with a  
185 capacity of 200 kN and a resolution of 0.1 kN for normal force is mounted on the  
186 bottom of each hydraulic cylinder. A strain gauge-type displacement transducer (NDT in  
187 Figure 3a) with a capacity of 50 mm and a resolution of 0.05 mm for normal distance is  
188 attached to the normal loading shaft, through which a normal force is transmitted from  
189 each hydraulic cylinder to the upper face of the sample block. Among the three  
190 cylinders, that on the right was only used to press the small samples in the present study.  
191 Data from all sensors (shear load, shear displacement, normal load and normal  
192 displacement) during the experiments are recorded using a 24 bit analog-to-digital

193 converter at a sampling rate of 24 kHz. This is typically decimated down to a lower

194 sampling rate (100 Hz in the present study) after the data acquisition.

195

## 196 **Friction experiments**

197 The friction experiments were performed using the bi-axial loading apparatus

198 describe above in double-direct shear configuration in which two 5 mm thick squared

199 plates were placed between a central and two side granite blocks, across contacting

200 interfaces with dimensions of 48 mm × 48 mm (inset in Figure 4a). Shear deformation

201 in the two plate samples was attained through the movement of the central block against

202 the stationary side blocks. The core samples were cut into squared plates, with the end

203 surfaces facing the granite blocks polished by using a high-precision surface grinding

204 machine to ensure flatness and parallelism within 12 µm. The surfaces of the three

205 granite blocks were ground and roughened with #14 SiC abrasive and to induce

206 deformation within the plate sample, and not along the boundary between the plate

207 sample and the granite block. Before insertion into the apparatus, the samples were

208 vacuumed and immersed in deionized water for greater than 16 hours, and this was

209 enough for the saturation of internal pores with water.

210 A series of velocity-stepping friction tests were conducted under atmospheric

211 conditions at normal stresses ranging from 2 MPa to 20 MPa. Note that although the

212 samples were initially water-saturated, they were not confined and exposed to air and

213 thus the saturation state could change due to shear-induced dilation or compaction of the

214 samples during the friction tests. These stresses simulated the ambient effective pressure

215 conditions at depths down to the bottom of the Anamizu Formation at 2 km, assuming

216 10 MPa/km from the bulk density of the samples and water density (1000 kg/m<sup>3</sup>) (Table

217 1). The normal stress ( $\sigma_n$ ) was maintained constant during sliding, while shear stress ( $\tau$ )

218 was increasing to deform the plate samples. The data on the normal and shear stresses,

219 shear displacement, and sample thickness were recorded at 100 Hz during the

220 experiments. After the start of the experiment, the plate samples were first sheared to a

221 displacement of 2 mm or higher at 1  $\mu\text{m}/\text{s}$  until the shear stress reached a steady state.

222 We then changed the sliding velocity in stepwise fashion from 0.1 to 100  $\mu\text{m}/\text{s}$  with at

223 least 0.3 mm displacement in each step, to evaluate the dependence of friction

224 parameters on velocity. After the experiments, the deformed plate samples were thin-

225 sectioned parallel to the shear direction in order to observe the microstructural changes

226 associated with different normal stresses using optical and scanning electron (JEOL

227 JSM-7001F) microscopes.

228 The velocity-stepping friction data were analyzed using an iterative least square

229 inversion modelling technique (e.g., Reinen and Weeks 1993; Blanpied et al. 1998) with

230 the Dieterich's rate and state friction law (aging) with one state variable (Dieterich

231 1979, 1981). In the constitutive law, the friction coefficient can be expressed as:

$$232 \quad \mu = \mu_0 + a \ln\left(\frac{V}{V_0}\right) + b \ln\left(\frac{V_0 \theta}{D_c}\right) \quad (1)$$

$$233 \quad \frac{d\theta}{dt} = 1 - \frac{V\theta}{D_c} \quad (2)$$

234 where  $\mu_0$  is steady-state friction coefficient at a reference velocity  $V_0$ ,  $V$  is sliding

235 velocity after the velocity step from  $V_0$ , respectively,  $\theta$  is state variable,  $D_c$  is critical slip

236 distance,  $a$  (direct effect) and  $b$  (evolution effect) are constants. At a steady state ( $d\theta/dt$

237 = 0, and then  $V\theta = D_c$ ), the friction coefficient is:

$$238 \quad \mu_{ss} = \mu_0 + (a - b) \ln\left(\frac{V}{V_0}\right) \quad (3)$$

239 Here, the velocity dependence of friction is given by  $(\mu_{ss} - \mu_0)/\ln(V/V_0) = (a - b)$ .

240 While a positive value of  $(a - b)$  represents velocity-strengthening promoting stable

241 fault slip, velocity weakening linked to a negative ( $a - b$ ) value is a necessity for the  
242 nucleation of unstable fault slip leading to earthquake generation (Marone 1998; Scholz  
243 1998). Since the elastic interaction between the fault friction and the apparatus  
244 surrounding the sample was considered in the modelling, we obtained optimized values  
245 of the friction parameters as well as the apparatus stiffness from the inversion technique  
246 using the Levenberg-Marquardt method (Reinen and Weeks 1993; Noda and  
247 Shimamoto 2009; Takahashi et al. 2011). Also, we eliminated the linear trend from the  
248 displacement-friction curve data before the inversion analysis.

249

## 250 **Results**

251 In the displacement vs shear stress curves of the tuff breccia samples deformed at  
252 normal stresses of 2 to 20 MPa, all samples exhibit a linear increase in shear stress to  
253 the yield point at a displacement of 1mm, followed by reaching to a residual constant or  
254 slightly increase trend at steady state (Figure 4a). Using data on the normal and shear  
255 stresses at displacements higher than 6 mm after the velocity step sequence, we  
256 constructed the Mohr Coulomb failure envelope for frictional behavior of our samples  
257 (Byerlee 1978; Handin 1969) using the following expression:

$$258 \quad \tau = C + \mu \cdot \sigma \quad (3)$$

where  $C$  is cohesive strength (Figure 4b). For the velocity dependence analysis, we

260 calculated the friction coefficient considering  $C = 0.22$  MPa derived from the linear

regression between the normal versus shear stresses, while apparent friction coefficient,

262 in which C is inevitably assumed to be zero, is frequently used for some rock friction

263 studies. The frictional strength of our breccia samples ranges between 0.40 and 0.47,

264 decreasing from the maximum to the minimum value with increasing normal stress

from 2 to 10 MPa, beyond which it increases to an intermediate value of 0.43 at 20 MPa

266 (Figure 4c).

Figure 5a shows friction response during the velocity step sequence (0.1–1–10–100

268  $\mu\text{m/s}$ ) at a range of normal stresses. A step increase or decrease in sliding velocity by an

order of magnitude after achieving steady state yields a friction response composed of

270 an instantaneous increase or decrease in friction by  $a \ln(V/V_0)$  and subsequent gradual

271 change by  $\ln(V/V_0)$  to a new steady state with increasing displacement, thereby

272 obeying the rate and state friction law (Figure 5b).

273 For the samples tested in the present study, a complex link exists between the

274 velocity dependence of friction and the normal stress (Figure 5c and Table 1). At a

275 normal stress of 2 MPa, we observe a wide range of  $(a - b)$  between -0.037 and 0.016.

276 When increasing normal stress up to 10 MPa, the samples exhibit a velocity-

277 strengthening behavior, with values of  $(a - b)$  ranging from neutral to 0.01. Then,  $(a -$

278  $b)$  decrease back to values of -0.002 to 0.005 at a normal stress of 20 MPa,

279 corresponding to the stress at 2 km depth.  $(a - b)$  tends to decrease from We observe a

280 decreasing trend in  $(a - b)$  with increasing normal stress except for data at 2 MPa where

281 there is significant scatter. For  $D_c$ , our data show no systematic trend with increasing

282 normal stress, although the range of the value becomes wider ( $\sim 60 \mu\text{m}$ ) at higher

283 normal stresses (Figure 5d). Also, whereas several studies have reported that these

284 friction parameters evolve with shear displacement (Mair and Marone, 1999; Saffer and

285 Marone, 2003), no clear dependence of them on displacement is documented in our data

286 (Table 1).

287 The deformed samples show monotonic microstructural change from localized

288 shear deformation to distributed cataclastic flow with increasing normal stress (Figure

289 6). For the sample deformed at 2 MPa, we observed a sharp boundary shear zone of  
290 more than 150  $\mu\text{m}$  width (this thickness is a minimum estimate because some grains can  
291 be lost during the thin section preparation) along the sample margin (Figure 6a). In this  
292 zone, substantial fracturing and attrition of angular phenocrysts of plagioclase produce  
293 gouge materials with grain sizes less than tens micrometers (Figure 6b). Because most  
294 of the shear strain imposed during the experiment is likely to be accommodated by the  
295 boundary shear zone, other parts of the sample lack an obvious imprint of shear  
296 deformation. As the normal stress becomes greater, the shear deformation zone widens  
297 toward the interior of the sample, and the plagioclase grains located inside the zone are  
298 cataastically deformed into small fragments aligned following the P orientation to  
299 form a distinct foliation (Logan et al. 1992; Passchier and Trouw 1998) (Figure 6c and  
300 6d). The brittle fracturing development observed in the deformed samples is dominantly  
301 in the plagioclase grains and rare in the pyroxene grains. For a normal stress of 20 MPa,  
302 the degree of deformation accommodated by the boundary shearing decreases  
303 significantly, and inversely, the disperse deformation characterized by cataclastic  
304 foliations are more frequent across the entire width of the sample and are occasionally

305 offset by Riedel micro shear zones. The shear zones are composed of fine-grained  
306 gouges (commonly < 20  $\mu\text{m}$ ) and their thickness is approximately a few hundred  
307 micrometers (Figure 6e and 6f). Both plagioclase and pyroxene grains are subjected to  
308 intense cataclasis under the high stress conditions.

309

#### 310 **4. Discussion**

311 Our experimental results examined the friction velocity dependence of friction in a  
312 range of normal stresses from 2 to 20 MPa for the sedimentary cover in the shallow part  
313 of the crust. The porous tuff breccia samples are characterized by predominantly  
314 velocity-strengthening behavior, and show slight decrease trend of the friction velocity  
315 dependence to neutral with increasing normal stress from 5 MPa to 20 MPa.  
316 Experimental studies have found that frictional velocity dependence varies with normal  
317 stress (e.g., Mair and Marone 1999; Saffer and Marone 2003; Niemeijer and Collettini  
318 2014; Carpenter et al. 2016; Sawai et al. 2016; Morrow et al. 2017). Data for powdered  
319 gouge prepared from kaolinite-rich claystone by Orellana et al. (2018) and smectite-rich  
320 natural fault gouge by Carpenter et al. (2015) have shown that mostly velocity-

321 strengthening behavior is apparent at normal stresses below 100 MPa, with some  
322 decreasing trend in  $(a - b)$  displayed at low normal stresses of less than 40 MPa. Our  
323 clay-poor samples indicate similar positive friction velocity dependence and its decrease  
324 with normal stress. In addition, friction experiments on a range of gouge materials by  
325 Ikari et al. (2011a) demonstrate a correlation between the velocity dependence of  
326 friction and the frictional strength. At coefficients of friction less than 0.5,  $(a - b)$  was  
327 always positive, which is roughly consistent with our results (Figure 4c).

328 Next, we discuss the relationship between the velocity-dependent frictional property  
329 and microstructures for our samples. Several studies have suggested that rocks  
330 exhibiting velocity-weakening behavior show localized shearing, whereas widely  
331 distributed deformation fabric is developed in those involving velocity-strengthening  
332 (Beeler et al. 1996; Mair and Marone 1999). Our deformed samples are characterized by  
333 a systematic change in deformation fabric from shear localization to distributed  
334 cataclastic flow as a function of normal stress (Figure 6), but we do not observe any  
335 apparent correlation between the microstructures and friction velocity dependence,  
336 suggested by previous observations. The sample at 2 MPa where most of shear occurs

337 in the boundary zone, shows some negative values of  $(a - b)$  but mainly velocity-

338 strengthening behavior. For the 20 MPa case where shear-localized Riedel shear zone

339 are developed, only one case of velocity weakening is observed. It is suggested that

340 Riedel shears may encourage the velocity-weakening behavior (Ikari et al. 2011b).

341 Although we believe that the microstructural localization/delocalization features seem

342 to have some partial correlation to the friction velocity dependence for our results,

343 further investigations are required to fully elucidate the mechanism responsible for the

344 stress-dependent frictional properties observed for the high porosity tuff breccia,

345 Our velocity-stepping friction experiments at elevated pressures provide a better

346 quantitative estimate of stress-variable, namely depth-variable, distribution of friction

347 velocity dependence in a shallow crustal zone for the Japan arc island, of which the

348 subsurface lithology is frequently dominated by unconsolidated thick sediment deposits,

349 and therefore some insight into its mechanical role for earthquake rupture dynamics.

350 With our results that the tuff breccia sample exhibits mostly frictionally stable,

351 velocity-strengthening behavior, we confirm the widely accepted hypothesis that a

352 shallow crustal layer behaves predominantly as a barrier for dynamic (unstable) rupture

353 propagation from the seismogenic zone during an earthquake. This explains the upper  
354 limit of the seismogenic zone width and the emergence of a shallow slip deficit (Wald  
355 and Heaton 1994; Simons et al. 2002; Fialko et al. 2005). The aftershock distribution of  
356 the 2007 Noto Hanto earthquake near the study area shows that the seismogenic zone is  
357 bounded upwardly by the about 2 km thick sediment layer composed of the Miocene  
358 volcaniclastic deposits including our sample (Kato et al. 2008), which is consistent with  
359 the seismically stable properties obtained in the experiments. Furthermore, for the 2004  
360 mid-Niigata prefecture earthquake also in the “Green Tuff” region, the associated  
361 surface slip was an order of magnitude lower than the slip at depth estimated from  
362 seismic data (Maruyama et al. 2005). This was interpreted as a shallow slip deficit due  
363 to thick sediment cover, and this is implicitly supported by our laboratory evidence.  
364 However, the present results at low slip rates do not exclude a possibility that  
365 earthquake rupture propagation could runaway through a shallow layer exhibiting  
366 velocity-strengthening at low slip rates when dynamic weakening mechanism is  
367 activated at coseismic slip rates (Di Toro et al. 2011; Noda and Lapusta 2013)  
368

369    **5. Conclusions**

370    To examine the frictional properties of a shallow sediment layer, we performed  
371    velocity-stepping friction tests on porous tuff breccia sample from the Miocene “Green  
372    Tuff” Formation, a major sediment cover in Japan, at normal stresses of 2 to 20 MPa.  
373    The experimental results document that the samples exhibit mostly velocity-  
374    strengthening behavior with a slightly decreasing trend in  $(a - b)$  with increasing normal  
375    stress. The frictionally stable properties are in accordance with the observations that the  
376    earthquakes occurred in the “Green Tuff” area are characterized by low seismicity and  
377    occurrence of shallow slip deficit in the shallow zone. Microstructural analyses on the  
378    postmortem samples reveal that the deformation fabric transitions from shear  
379    localization to distributed cataclastic flow with increasing normal stress. For our  
380    samples, however, we do not observe a clear relationship between microstructures and  
381    friction velocity dependence as previously reported. We suggest that laboratory  
382    investigations, as we present here, can illuminate detailed depth-variable distribution of  
383    friction velocity dependence of a shallow sediment layer. Our finding, taken together  
384    with further investigation on a variety of subsurface sediment materials, would facilitate

385 comprehensive understanding of the mechanical role of a shallow sediment layer for  
386 earthquake rupture dynamics and shallow seismicity.

387

## 388 **Declarations**

### 389 **Availability of data and materials**

390 All experimental raw data are publicly available in a repository (at  
391 <https://zenodo.org/record/4047766#.X31NZmgzaUk>).

392

### 393 **Competing interests**

394 The authors declare that they have no competing interests.

395

### 396 **Funding**

397 This study was financially supported by the general operating expenses of the Central  
398 Research Institute of Electric Power Industry (CRIEPI).

399

### 400 **Authors' contributions**

401 KM planned the study, interpreted the experimental data, and drafted the manuscript.

402 SU and SI performed the friction experiments and analyzed data. TH contributed to the

403 microstructural analysis of the samples and provided useful discussions. All authors

404 read and approved the final manuscript.

405

#### 406 **Acknowledgments**

407 We acknowledge the Hokuriku Electric Power Co., Ltd. for providing fresh core

408 samples used for the friction experiments. We are grateful to T. Iida and T. Taniguchi for

409 assisting with the experiments and thin section preparation. Figures were drawn using

410 Generic Mapping Tools (Wessel et al. 2013).

411

#### 412 **References**

413 Beeler NM, Tullis TE, Blanpied ML, Weeks JD (1996) Frictional behavior of large

414 displacement experimental faults. J Geophys Res 101:8697– 8715.

415 doi:10.1029/96JB00411

- 416 Blanpied ML, Lockner DA, Byerlee JD (1991) Fault stability inferred from granite
- 417 sliding experiments at hydrothermal conditions. *Geophys Res Lett* 18:609–612.
- 418 doi:10.1029/91gl00469
- 419 Blanpied ML, Marone CJ, Lockner DA, Byerlee JD, King DP (1998) Quantitative
- 420 measure of the variation in fault rheology due to fluid-rock interactions. *J Geophys*
- 421 *Res* 103:9691– 9712. doi:10.1029/98JB00162
- 422 Boulton C, Carpenter BM, Toy V, Marone C (2012) Physical properties of surface
- 423 outcrop cataclastic fault rock, Alpine Fault, New Zealand. *Geochem Geophys*
- 424 *Geosyst* 13:Q01018. doi:10.1029/2011GC003872
- 425 Brune JN, Anooshehpoor A (1998) A physical model of the effect of a shallow weak
- 426 layer on strong ground motion for strike-slip ruptures. *Bull Seismol Soc Am*
- 427 88:1070–1078. doi:10.2172/776519
- 428 Byerlee J (1978) Friction of rocks. *Pure and Appl Geophys* 116:615–626.
- 429 doi:10.1007/BF00876528

- 430 Carpenter BM, Marone C, Saffer DM (2011) Weakness of the San Andreas Fault  
431 revealed by samples from the active fault zone. *Nat Geosci* 4:251–254.  
432 doi:10.1038/NGEO1089
- 433 Carpenter BM, Saffer DM, Marone C (2015) Frictional properties of the active San  
434 Andreas Fault at SAFOD: Implications for fault strength and slip behavior. *J  
435 Geophys Res* 120:5273–5289. doi:10.1002/2015JB011963
- 436 Carpenter BM, Collettini C, Viti C, Cavallo A (2016) The influence of normal stress  
437 and sliding velocity on the frictional behavior of calcite at room temperature:  
438 insights from laboratory experiments and microstructural observations. *Geophys J  
439 Int* 205:548–561. doi:10.1093/gji/ggw038
- 440 Das S, Scholz CH (1983) Why large earthquakes do not nucleate at shallow depths.  
441 *Nature* 305:621–623. doi:10.1038/305621a0
- 442 Day SM, Ely GP (2002) Effect of a shallow weak zone on fault rupture: numerical  
443 simulation of scale-model experiments. *Bull Seismol Soc Am* 92:3022–3041
- 444 Dieterich JH (1979) Modeling of rock friction, 1. Experimental results and constitutive  
445 equations. *J Geophys Res* 84:2161–2168. doi:10.1029/JB084iB05p02161

- 446 Dieterich JH (1981) Constitutive properties of faults with simulated gouge. In: Carter
- 447 NL, Friedman M, Logan JM and Stearns DW (eds) Mechanical Behavior of Crustal
- 448 Rocks, Geophysical Monograph Series, vol 24. American Geophysical Union,
- 449 Washington, D.C., pp 103–120. doi:10.1029/GM024p0103
- 450 Di Toro G, Han R, Hirose T, Paola ND, Nielsen S, Mizoguchi K, Ferri F, Cocco M,
- 451 Shimamoto T (2011) Fault lubrication during earthquakes. *Nature* 471:494–498.
- 452 doi:10.1038/nature09838
- 453 Doser DI, Kanamori H (1986) Depth of seismicity in the Imperial Valley region (1977–
- 454 1983) and its relationship to heat flow, crustal structure and the October 15, 1979
- 455 earthquake. *J Geophys Res* 91:675–688. doi:10.1029/JB091iB01p00675
- 456 Fialko Y, Sandwell D, Simons M, Rosen P (2005) Three-dimensional deformation
- 457 caused by the Bam, Iran, earthquake and the origin of shallow slip deficit. *Nature*
- 458 435:295–299. doi:10.1038/nature03425
- 459 Fredrich JT, Evans B, Wong T-F (1989) Micromechanics of the brittle to plastic
- 460 transition in Carrara marble. *J Geophys Res* 94:4129–4145.
- 461 doi:10.1029/JB094iB04p04129

- 462 Fujiwara T, Kodaira S, No T, Kaiho Y, Takahashi N, Kaneda Y (2011) The 2011
- 463 Tohoku-Oki earthquake: displacement reaching the trench axis. *Science* 334:1240.
- 464 doi:10.1126/science.1211554
- 465 Handin J (1969) On the Coulomb-Mohr failure criterion. *J Geophys Res* 74:5343–5348.
- 466 doi:10.1029/JB074i022p05343
- 467 Huzioka K (1963) Geology of the Green Tuff region in Japan. *Mining Geology* 13:358–375 (in Japanese). doi:10.11456/shigenchishitsu1951.13.62\_358
- 469 Hyndman RD, Yamano M, Oleskevich DA (1997) The seismogenic zone of subduction
- 470 thrust faults. *Island Arc* 6:244–260. doi:10.1111/j.1440-1738.1997.tb00175.x
- 471 Ikari MJ, Marone C, Saffer DM (2011a) On the relation between fault strength and
- 472 frictional stability. *Geology* 39:83–86. doi:10.1130/G31416.1
- 473 Ikari MJ, Niemeijer AR, Marone C (2011b) The role of fault zone fabric and
- 474 lithification state on frictional strength, constitutive behavior, and deformation
- 475 microstructure. *J Geophys Res* 116:B08404. doi:10.1029/2011JB008264

- 476 Ikari MJ, Ito Y, Ujiie K, Kopf AJ (2015) Spectrum of slip behaviour in Tohoku fault
- 477 zone samples at plate tectonic slip rates. *Nat Geosci* 8:870–874.
- 478 doi:10.1038/ngeo2547
- 479 Ito K (1999) Seismogenic layer, reflective lower crust, surface heat flow and large
- 480 inland earthquakes. *Tectonophysics* 306:423–433. doi:10.1016/S0040-
- 481 1951(99)00069-4
- 482 Ito Y, Tsuji T, Osada Y, Kido M, Inazu D, Hayashi Y, Tsushima H, Hino R, Fujimoto
- 483 H (2011) Frontal wedge deformation near the source region of the 2011 Tohoku-
- 484 oki earthquake. *Geophys Res Lett* 38. doi:10.1029/2011GL048355
- 485 Kaneko Y, Fialko Y (2011) Shallow slip deficit due to large strike-slip earthquakes in
- 486 dynamic rupture simulations with elasto-plastic off-fault response. *Geophys J Int*
- 487 186:1389–1403. doi:10.1111/j.1365-246X.2011.05117.x
- 488 Kano K, Uto K, Ohguchi T (2007) Stratigraphic review of Eocene to Oligocene
- 489 successions along the eastern Japan Sea: Implication for early opening of the Japan
- 490 Sea. *J Asian Earth Sci* 30:20–32. doi:10.1016/j.jseaes.2006.07.003

- 491 Kaseno Y (1965) Geology of the Noto Peninsula. In Science Research. Report of the
- 492 Noto Peninsula (Gakujutsu Chosa Hokokusho). Ishikawa Prefectural Government,
- 493 Kanazawa, Japan (**in Japanese with English abstract**)
- 494 Kato A, Sakai S, Iidaka T, Iwasaki T, Kurashimo E, Igarashi T, Hirata N, Kanazawa T,
- 495 Group for the aftershock observations of the 2007 Noto Hanto Earthquake (2008)
- 496 Three-dimensional velocity structure in the source region of the Noto Hanto
- 497 Earthquake in 2007 imaged by a dense seismic observation. *Earth Planets Space*
- 498 60:105–110. doi:10.1186/BF03352769
- 499 Kikuchi Y, Tono S, Funayama M (1991) Petroleum resources in the Japanese island-arc
- 500 setting. *Episodes* 14:236–241. doi:10.18814/epiiugs/1991/v14i3/007
- 501 Kodaira S, No T, Nakamura Y, Fujiwara T, Kaiho Y, Miura S, Takahashi N, Kaneda Y,
- 502 Taira A (2012) Coseismic fault rupture at the trench axis during the 2011 Tohoku-
- 503 oki earthquake. *Nat Geosci* 5:646–650. doi:10.1038/ngeo1547
- 504 Logan JM, Dengo CA, Higgs NG, Wang ZZ (1992) Fabrics of experimental fault zones:
- 505 Their development and relationship to mechanical behavior. In: Evans B, Wong T-

- 506 F (eds) Fault Mechanics and Transport Properties of Rocks, Academic Press, San
- 507 Diego, CA, pp 33–67. doi:10.1016/S0074-6142(08)62814-4
- 508 Maggi A, Jackson J, McKenzie D, Priestley K (2000) Earthquake focal depths, effective
- 509 elastic thickness, and the strength of the continental lithosphere. *Geology* 28:495–
- 510 498. doi:10.1130/0091-7613(2000)28<495:EFDEET>2.0.CO;2
- 511 Mair K, Marone C (1999) Friction of simulated fault gouge for a wide range of
- 512 velocities and normal stresses. *J Geophys Res* 104:28,899–28,914.
- 513 doi:10.1029/1999JB900279
- 514 Marone C (1998) Laboratory-derived frictional laws and their application to seismic
- 515 faulting. *Annu Rev Earth Planet Sci* 94:12321–12335.
- 516 doi:10.1146/annurev.earth.26.1.643
- 517 Marone C, Scholz CH (1988) The depth of seismic faulting and the upper transition
- 518 from stable to unstable slip regimes. *Geophys Res Lett* 15:621–624.
- 519 doi:10.1029/GL015i006p00621
- 520 Marone C, Scholz CH, Bilham R (1991) On the mechanics of earthquake afterslip. *J*
- 521 *Geophys Res* 96:8441–8452. doi:10.1029/91JB00275

- 522 Maruyama T, Fusejima Y, Yoshioka T, Awata Y, Matsu'ura T (2005) Characteristics of  
523 the surface rupture associated with the 2004 Mid Niigata Prefecture earthquake,  
524 central Japan and their seismotectonic implications. *Earth Planets Space* 57:521–  
525 526. doi:10.1186/BF03352586
- 526 Matsuda T (1977) Estimation of future destructive earthquakes from active faults on  
527 land in Japan. *J Phys Earth* 25:S251–S260.  
528 doi:10.4294/jpe1952.25.Supplement\_S251
- 529 Moore GF, Bangs NL, Taira A, Kuramoto S, Pangborn E, Tobin HJ (2007) Three-  
530 dimensional splay fault geometry and implications for Tsunami generation. *Science*  
531 318:1128–1131. doi:10.1126/science.1147195
- 532 Morrow CA, Moore DE, Lockner DA (2017) Frictional strength of wet and dry  
533 montmorillonite. *J Geophys Res* 122:3392–3409. doi:10.1002/2016JB013658
- 534 Murata Y, Kano K (1995) The areas of the geologic units comprising the Japanese  
535 Islands, calculated by using the Geological Map of Japan 1:1,000,000, 3rd Edition,  
536 CD-ROM version. *Chishitsu News* 493:26–29 (**in Japanese**)

- 537 Nazareth JJ, Hauksson E (2004) The Seismogenic Thickness of the Southern California
- 538 Crust. Bull Seismol Soc Am 94:940–960. <http://doi.org/10.1785/0120020129>
- 539 Niemeijer AR, Collettini C (2014) Frictional properties of a low-angle normal fault
- 540 under in situ conditions: Thermally-activated velocity weakening. Pure and Appl
- 541 Geophys 171:2641–2664. doi:10.1007/s00024-013-0759-6
- 542 Niemeijer AR, Boulton C, Toy VG, Townend J, Sutherland R (2016) Large-
- 543 displacement, hydrothermal frictional properties of DFDP-1 fault rocks, Alpine
- 544 Fault, New Zealand: Implications for deep rupture propagation. J Geophys Res
- 545 121:624–647. doi:10.1002/2015JB012593
- 546 Noda H, Lapusta N (2013) Stable creeping fault segments can become destructive as a
- 547 result of dynamic weakening, Nature 493:518–521. doi:10.1038/nature11703
- 548 Noda H, Shimamoto T (2009) Constitutive properties of clayey fault gouge from the
- 549 Hanaore fault zone, southwest Japan. J Geophys Res 114:B04409.
- 550 doi:10.1029/2008JB005683

- 551 Orellana LF, Scuderi MM, Collettini C, Violay M (2018) Frictional properties of
- 552 Opalinus Clay: implications for nuclear waste storage. *J Geophys Res* 123:157–
- 553 175. doi:10.1002/2017JB014931
- 554 Ozaki M, Komazawa M, Inoue T (2010) 1:2000,000 Geological Map with Gravity
- 555 Contours in and around the Northern Part of Noto Peninsula. In *Seamless*
- 556 *Geoinformation of Coastal Zone “Nothern Coastal Zone of Noto Peninsula”*
- 557 (Digital Geoscience Map S-1). Geological survey of Japan, AIST, Tsukuba.
- 558 <https://www.gsj.jp/researches/project/coastal-geology/results/s-1.html>. Accessed 23
- 559 Dec 2020
- 560 Passchier CW, Trouw RAJ (1998) *Microtectonics*. Springer, Berlin. doi:10.1007/978-3-
- 561 662-08734-3
- 562 Pitarka A, Dalguer L A, Day SM, Somerville PG, Dan K (2009) Numerical study of
- 563 ground-motion differences between buried-rupturing and surface-rupturing
- 564 earthquakes. *Bull Seismol Soc Am* 99:1521–1537. doi:10.1785/0120080193

- 565 Reinen LA, Weeks JD (1993) Determination of rock friction constitutive parameters
- 566 using an iterative least squares inversion method. *J Geophys Res* 98:15937–15950.
- 567 doi:10.1029/93JB00780
- 568 Rice JR (1993) Spatio-temporal complexity of slip on a fault. *J Geophys Res* 98:9885–
- 569 9907. doi:10.1029/93JB00191
- 570 Ruina A (1983) Slip instability and state variable friction laws. *J Geophys Res*
- 571 88:10,359–10,370. doi:10.1029/JB088iB12p10359
- 572 Saffer DM, Marone C (2003) Comparison of smectite- and illite-rich gouge frictional
- 573 properties: application to the updip limit of the seismogenic zone along subduction
- 574 megathrusts. *Earth and Planet Sci Lett* 215:219–235. doi:10.1016/S0012-
- 575 821X(03)00424-2
- 576 Sato H, Amano K (1991) Relationship between tectonics, volcanism, sedimentation and
- 577 basin development, Late Cenozoic, central part of Northern Honshu, Japan.
- 578 *Sediment Geol* 74:323–343. doi:10.1016/0037-0738(91)90071-K

- 579 Sawai M, Niemeijer AR, Plümper O, Hirose T, Spiers CJ (2016) Nucleation of  
580 frictional instability caused by fluid pressurization in subducted blueschist.
- 581 Geophys Res Lett 43:2543–2551. doi:10.1002/2015GL067569
- 582 Sawai M, Niemeijer AR, Hirose T, Spiers CJ (2017) Frictional properties of JFAST  
583 core samples and implications for slow earthquakes at the Tohoku subduction zone.
- 584 Geophys Res Lett 44:8822–8831. doi:10.1002/2017GL073460
- 585 Scholz CH (1998) Earthquakes and friction laws. Nature 391:37–42. doi:10.1038/34097
- 586 Sibson RH (1982) Fault zone models, heat flow, and the depth distribution of  
587 earthquakes in the continental crust of the United States. Bull Seismol Soc Am  
588 72:151-163
- 589 Sibson RH (1983) Continental fault structure and the shallow earthquake source. J Geol  
590 Soc London 140:741–767. doi:10.1144/gsjgs.140.5.0741
- 591 Simons M, Fialko Y, Rivera L (2002) Coseismic deformation from the 1999  $M_w$  7.1  
592 Hector Mine, California, earthquake as inferred from InSAR and GPS observations.
- 593 Bull Seismol Soc Am 92:1390–1402

- 594 Somerville PG (2003) Magnitude scaling of the near fault rupture directivity pulse.
- 595 Phys Earth Planet Inter 137:201–212. doi:10.1016/S0031-9201(03)00015-3
- 596 Takahashi M, Uehara S, Mizoguchi K, Shimizu I, Okazaki K, Masuda K (2011) On the
- 597 transient response of serpentine (antigorite) gouge to stepwise changes in slip
- 598 velocity under high-temperature conditions. J Geophys Res 116: B10405.
- 599 doi:10.1029/2010JB008062
- 600 Tse ST, Rice R (1986) Crustal earthquake instability in relation to the depth variation of
- 601 frictional slip properties. J Geophys Res 91:9452–9472.
- 602 doi:10.1029/JB091iB09p09452
- 603 Ujiie K, Tanaka H, Saito T, Tsutsumi A, Mori JJ, Kameda J, Brodsky EE, Chester FM,
- 604 Eguchi N, Toczko S, Expedition 343 and 343 T Scientists (2013) Low coseismic
- 605 shear stress on the Tohoku-Oki megathrust determined from laboratory
- 606 experiments. Science 342:12111-1214. doi:10.1126/science.1243485
- 607 Verberne BA, He C, Spiers CJ (2010) Frictional properties of sedimentary rocks and
- 608 natural fault gouge from the Longmenshan Fault Zone, Sichuan, China. Bull
- 609 Seismol Soc Am 100:2767–2790. <http://dx.doi.org/10.1785/0120090287>

- 610 von Huene R, Langseth M, Nasu N, Okuda H (1982) A summary of Cenozoic tectonic  
611 history along the IPOD Japan Trench transect. *Geol Soc Am Bull* 93:829–846.  
612 doi:10.1130/0016-7606(1982)93<829:ASOCTH>2.0.CO;2
- 613 Wald DJ, Heaton TH (1994) Spatial and temporal distribution of slip for the 1992  
614 Landers, California, earthquake. *Bull Seismol Soc Am* 84:668–691
- 615 Wesnousky SG, Scholz CH, Shimazaki K, Matsuda T (1984) Integration of geological  
616 and seismological data for the analysis of seismic hazard: A case study of Japan.  
617 *Bull Seismol Soc Am* 74:687–708
- 618 Wessel P, Smith WHF, Scharroo R, Luis JF, Wobbe F (2013) Generic Mapping Tools:  
619 Improved version released. *Eos Trans Am Geophys Union* 94:409–410.  
620 doi:10.1002/2013EO450001
- 621 Zinke R, Hollingsworth J, Dolan JF (2014) Surface slip and off-fault deformation  
622 patterns in the 2013 M<sub>w</sub> 7.7 Balochistan, Pakistan earthquake: Implications for  
623 controls on the distribution of near-surface coseismic slip. *Geochem Geophys  
624 Geosyst* 15:5034–5050. doi:10.1002/2014GC005538
- 625

626 **Table 1** List of optimized values of the friction parameters from inversion modeling for

627 all experiments.

628

Run No.	Normal	Velocity	Shear		$a$	$a. s.d.^a$	$b$	$b. s.d.^a$	$D_c$	$D_c. s.d.^a$	$a - b$
	Stress	step	Disp.	(mm)					( $\mu\text{m}$ )	( $\mu\text{m}$ )	
	(MPa)	( $\mu\text{m}/\text{s}$ )									
BASH155-01	2	1 to 0.1	2.96	0.0016	0.00096	0.0047	0.00044	16.2	8.54	-0.0030	
BASH155-02	2	0.1 to 1	3.49	0.0233	0.00504	0.0075	0.00028	27.2	1.41	0.0158	
BASH155-03	2	1 to 10	3.99	0.0120	0.00158	0.0083	0.00019	28.9	1.27	0.0037	
BASH155-04	2	10 to 100	4.28	0.0127	0.00355	0.0125	0.00103	26.3	3.49	0.0002	
BASH155-05	2	100 to 10	4.58	0.0133	0.00360	0.0129	0.00121	10.6	2.16	0.0003	
BASH155-06	2	10 to 1	4.89	0.0062	0.00061	0.0086	0.00030	11.5	0.83	-0.0024	
BASH155-07	2	1 to 0.1	5.39	0.0011	0.00069	0.0038	0.00036	21.3	13.6	-0.0026	
BASH155-08	2	0.1 to 1	5.92	0.0173	0.00264	0.0093	0.00019	15.2	0.45	0.0080	
BASH155-09	2	1 to 10	6.42	0.0122	0.00141	0.0094	0.00029	13.1	0.61	0.0028	
BASH155-10	2	10 to 100	6.72	0.0145	0.00392	0.0105	0.00155	14.5	2.92	0.0040	
BASH155-11	2	100 to 10	4.05	0.0080	0.00244	0.0117	0.00078	16.4	2.89	-0.0037	
BASH155-12	2	10 to 1	7.35	0.0026	0.00045	0.0061	0.00018	20.5	2.49	-0.0034	
BASH156-01	5	1 to 0.1	2.92	0.0053	0.00005	0.0017	0.00001	14.5	0.76	0.0036	
BASH156-02	5	0.1 to 1	3.45	0.0234	0.00047	0.0163	0.00050	2.0	0.06	0.0071	
BASH156-03	5	1 to 10	3.96	0.0157	0.00023	0.0097	0.00025	4.1	0.13	0.0060	
BASH156-04	5	10 to 100	4.25	0.0390	0.00088	0.0328	0.00089	1.5	0.05	0.0062	
BASH156-05	5	100 to 10	4.54	0.0095	0.00011	0.0058	0.00004	35.0	0.51	0.0037	
BASH156-06	5	10 to 1	4.86	0.0053	0.00007	0.0036	0.00004	21.8	0.38	0.0017	
BASH156-07	5	1 to 0.1	5.36	0.0056	0.00004	0.0024	0.00002	61.9	0.62	0.0032	
BASH156-08	5	0.1 to 1	5.90	0.0195	0.00017	0.0091	0.00012	2.8	0.04	0.0104	
BASH156-09	5	1 to 10	6.39	0.0222	0.00079	0.0151	0.00084	2.5	0.14	0.0071	
BASH156-10	5	10 to 100	6.69	0.0166	0.00056	0.0106	0.00057	5.3	0.36	0.0060	
BASH156-11	5	100 to 10	7.10	0.0079	0.00007	0.0060	0.00003	32.8	0.36	0.0019	
BASH156-12	5	10 to 1	7.41	0.0069	0.00006	0.0042	0.00003	26.8	0.35	0.0027	
BASH153-01	10	1 to 0.1	1.91	0.0118	0.00180	0.0056	0.00150	0.1	0.02	0.0063	
BASH153-02	10	0.1 to 1	2.45	0.0135	0.00034	0.0048	0.00015	5.5	0.17	0.0087	
BASH153-03	10	1 to 10	2.95	0.0657	0.00004	0.0599	0.00071	0.4	0.05	0.0058	
BASH153-04	10	10 to 100	3.24	0.0114	0.00343	0.0066	0.00254	11.3	6.30	0.0048	
BASH153-05	10	100 to 10	3.52	0.0057	0.00058	0.0051	0.00023	31.0	2.77	0.0007	
BASH153-06	10	10 to 1	3.83	0.0047	0.00029	0.0033	0.00011	32.8	2.88	0.0014	
BASH153-07	10	1 to 0.1	4.33	0.0041	0.00032	0.0022	0.00013	47.9	7.68	0.0019	
BASH153-08	10	0.1 to 1	4.87	0.0310	0.01481	0.0259	0.01486	0.8	0.46	0.0051	
BASH153-09	10	1 to 10	5.37	0.0163	0.00264	0.0105	0.00278	4.1	1.20	0.0058	
BASH153-10	10	10 to 100	5.67	0.0113	0.00328	0.0078	0.00243	9.4	4.50	0.0036	
BASH153-11	10	100 to 10	5.98	0.0065	0.00080	0.0056	0.00031	24.2	2.92	0.0009	
BASH153-12	10	10 to 1	6.30	0.0064	0.00038	0.0042	0.00013	30.7	2.03	0.0022	

BASH157-01	20	1 to 0.1	2.90	0.0051	0.00002	0.0024	0.00001	66.6	0.86	0.0027
BASH157-02	20	0.1 to 1	3.44	0.0277	0.00024	0.0222	0.00025	2.1	0.02	0.0055
BASH157-03	20	1 to 10	3.94	0.0117	0.00007	0.0065	0.00006	9.3	0.12	0.0051
BASH157-04	20	10 to 100	4.23	0.0111	0.00028	0.0077	0.00019	13.5	0.48	0.0034
BASH157-05	20	100 to 10	4.63	0.0069	0.00007	0.0066	0.00003	40.4	0.38	0.0003
BASH157-06	20	10 to 1	4.94	0.0062	0.00003	0.0049	0.00001	46.6	0.23	0.0014
BASH157-07	20	1 to 0.1	5.44	0.0056	0.00002	0.0029	0.00001	55.0	0.19	0.0026
BASH157-08	20	0.1 to 1	5.98	0.0157	0.00039	0.0103	0.00041	3.5	0.15	0.0053
BASH157-09	20	1 to 10	6.48	0.0102	0.00009	0.0071	0.00007	7.3	0.12	0.0031
BASH157-10	20	10 to 100	6.77	0.0124	0.00042	0.0091	0.00034	8.4	0.48	0.0033
BASH157-11	20	100 to 10	7.05	0.0048	0.00006	0.0065	0.00002	37.8	0.31	-0.0017
BASH157-12	20	10 to 1	7.37	0.0055	0.00003	0.0049	0.00001	33.4	0.21	0.0006

<sup>a</sup>Standard deviation of friction parameters.

629

630

### 631 **Figure captions**

632 **Figure 1** Map of the Japan island arc showing distribution of the Green Tuff Formation

633 (dotted area), after Huzioka (1963). The stars represent the epicenters of the 2004 M6.6

634 Niigata Chuetsu earthquake (2004NC), the 2007 M6.6 Niigata Chuetsu-oki earthquake

635 (2007NCO), and the 2007 M6.7 Noto Hanto earthquake (2007NH). The upper left inset

636 shows the volcaniclastic rocks distribution of the Green Tuff Formation in the Noto

637 Peninsula (Kaseno 1965). The Andesitic rocks indicated by the gray areas represent the

638 Anamizu Formation, where the tuff breccia samples for the experiments were collected.

639 The open circle shows the locations drilled for sampling. The position of the inset is

640 given by the block box in the main figure.

641

642 **Figure 2** Porous tuff breccia sample used in the experiments **a** Photomicrograph of the  
643 tuff breccia sample under planed-polarized light. **b** X-ray diffraction pattern of the  
644 experimental sample. The X-ray diffraction analysis was done under the following  
645 conditions: anode is Cu, acceleration voltage is 40 kV, current is 20 mA, step size is  
646 0.02°, and scan speed is 2°/min. Pl, plagioclase; Opx, orthopyroxene; Cpx,  
647 clinopyroxene; Sm, smectite; Hem, hematite.

648

649 **Figure 3** The bi-axial double direct shear loading apparatus (BASH). **a** Schematic  
650 diagram showing a biaxial compression apparatus built at CRIEPI, involving the sample  
651 assembly in double-direct shear configuration for a 50 cm long rock specimen. **b** single-  
652 direct shear sample assembly for the long specimen. **c** double-direct shear sample  
653 assembly for short rock specimens used in this study. The assembly was used in this  
654 study. SLC, shear load cell; SDT, shear displacement transducer; NLC, normal load cell;  
655 NDT, normal displacement transducer; AC, accumulator; EMC, electromagnetic clutch.

656

657   **Figure 4** Mechanical data from velocity-stepping experiments conducted at elevated  
658   normal stress. **a** Shear stress versus shear displacement for the samples deformed at 2  
659   (orange), 5 (green), 10 (red) and 20 MPa (blue). The upper left inset displays a  
660   schematic of double-direct shear configuration. **b** Steady state shear stress for shear  
661   displacement > 6mm as a function of the normal stress. Friction coefficient and  
662   cohesive strength determined by a least square fit (coefficient of determination R<sup>2</sup> =  
663   0.9975) with the Mohr Coulomb linear equation (dash lines) were 0.43 ( $\pm 0.02$ ) and 0.22  
664   ( $\pm 0.17$ ), respectively. **c** Steady state friction coefficient corrected for the cohesive  
665   strength (0.22 MPa) as a function of normal stress.

666

667   **Figure 5** Experimental data and its friction parameter modeling results. **a** Friction as a  
668   function of shear displacement with velocity steps between 0.1 and 100  $\mu\text{m/s}$  at normal  
669   stresses of 2, 5, 10 and 20 MPa. Curves are offset vertically for clarity. **b** Example of  
670   friction response to a velocity step from 1 to 10  $\mu\text{m/s}$  (gray) with a best-fitting curve  
671   obtained from inversion analysis (red). **c** Velocity-dependent friction parameter ( $a - b$ )  
672   and **d** critical slip distance  $D_c$  plotted as a function of normal stress for all velocity steps

673 (blue circle, 0.1  $\mu\text{m/s}$ ; red square, 1  $\mu\text{m/s}$ ; green triangle, 10  $\mu\text{m/s}$ ; orange diamond, 100  
674  $\mu\text{m/s}$ ).

675

676 **Figure 6** Microstructures of the deformed samples after the velocity-stepping friction  
677 tests at normal stresses of **a**, **b** 2 MPa, **c**, **d** 10 MPa and **e**, **f** 20 MPa, under optical (**a**, **c**,  
678 **f**) and electron (**b**, **d**, **f**) microscopes. Shear sense is top-to-the-left. **a** The boundary  
679 shear zone (BZ), of which the lower boundary is delimited by the dotted white line, is  
680 located along the upper edge of the sample. The block box gives the position of **b**. **b** A  
681 close-up view of the boundary shear zone characterized by < 20  $\mu\text{m}$  small grains,  
682 located above the dotted yellow line. **c** The dotted lines indicate cataclastic P foliations  
683 formed in upper part of the sample. The block box gives the position of **d**. **d** A close-up  
684 view of elongated plagioclase fragments, demarcated by the dotted yellow line, forming  
685 the cataclastic foliations. **e** The P foliations (dotted lines) are pervasive across the bulk  
686 sample, sometimes offset by left-lateral Riedel shears (Solid white line). The block box  
687 gives the position of **f**. **f** A close-up view of the Riedel micro shear zone bounded by the  
688 dotted yellow lines. Pl, plagioclase; Opx, orthopyroxene; Cpx, clinopyroxene; Hem,

689    Hematite.

690

## Figures

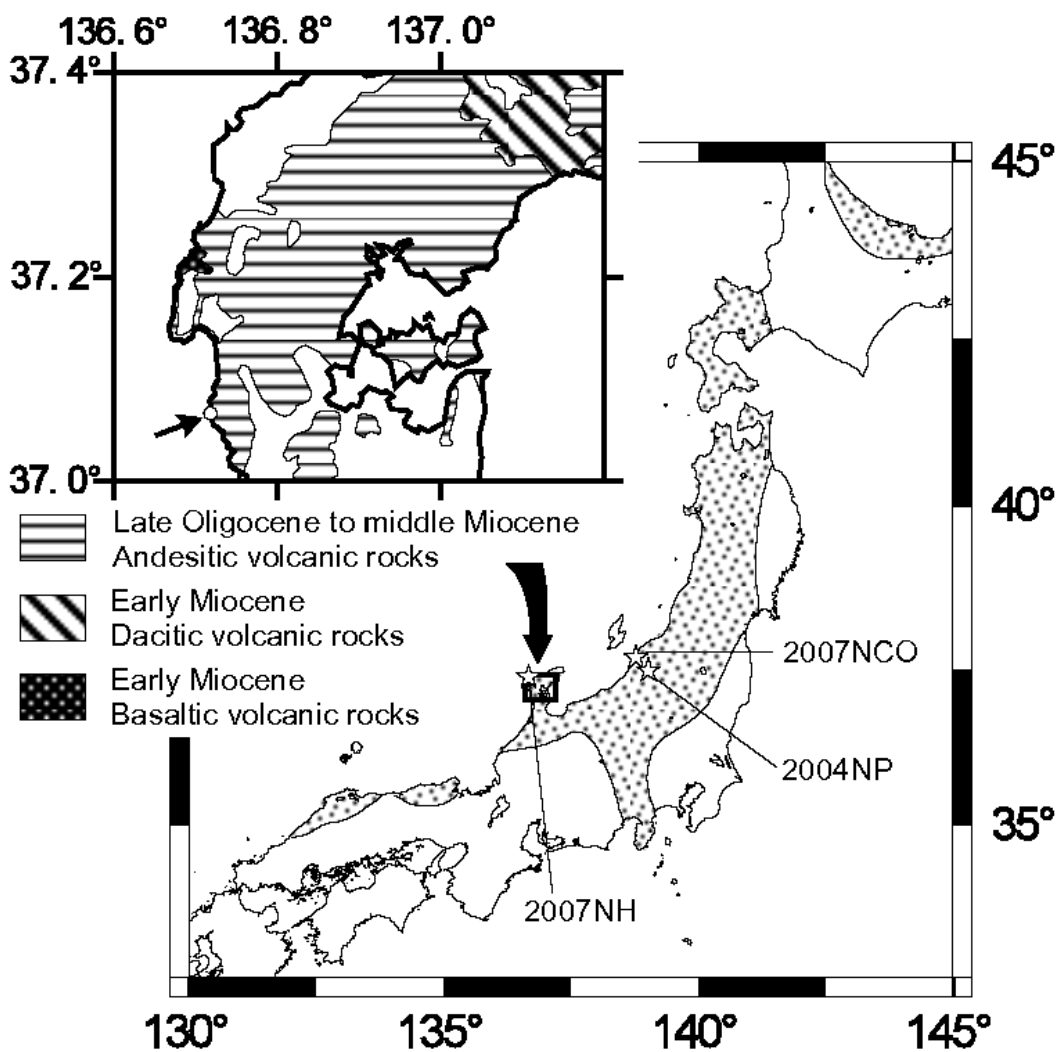
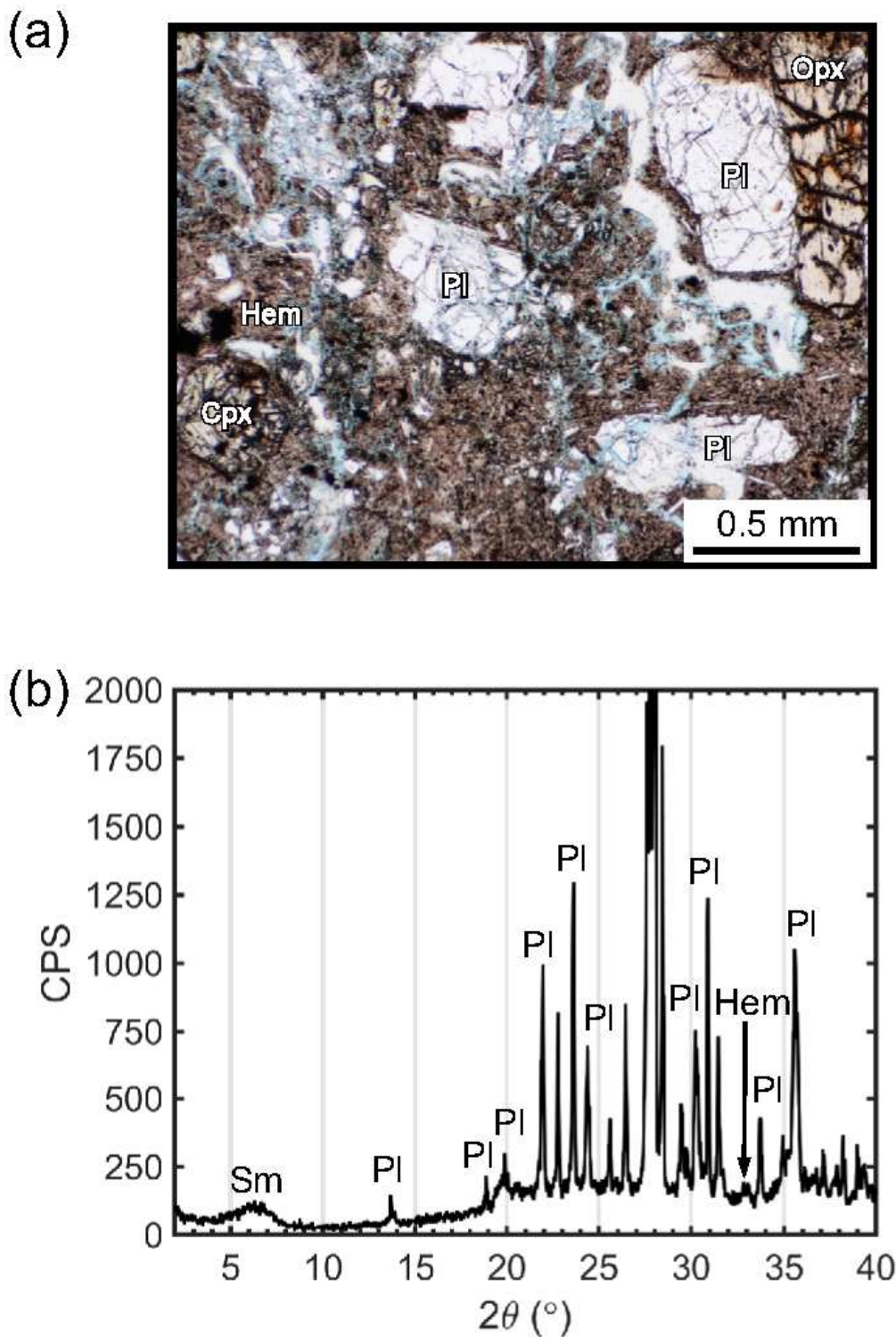


Figure 1

Map of the Japan island arc showing distribution of the Green Tuff Formation (dotted area), after Huzioka (1963). The stars represent the epicenters of the 2004 M6.6 Niigata Chuetsu earthquake (2004NC), the 2007 M6.6 Niigata Chuetsu-oki earthquake (2007NCO), and the 2007 M6.7 Noto Hanto earthquake (2007NH). The upper left inset shows the volcaniclastic rocks distribution of the Green Tuff Formation in the Noto Peninsula (Kaseno 1965). The Andesitic rocks indicated by the gray areas represent the Anamizu Formation, where the tuff breccia samples for the experiments were collected. The open circle shows the locations drilled for sampling. The position of the inset is given by the block box in the main figure. Note: The designations employed and the presentation of the material on this map do not imply the expression of any opinion whatsoever on the part of Research Square concerning the legal

status of any country, territory, city or area or of its authorities, or concerning the delimitation of its frontiers or boundaries. This map has been provided by the authors.

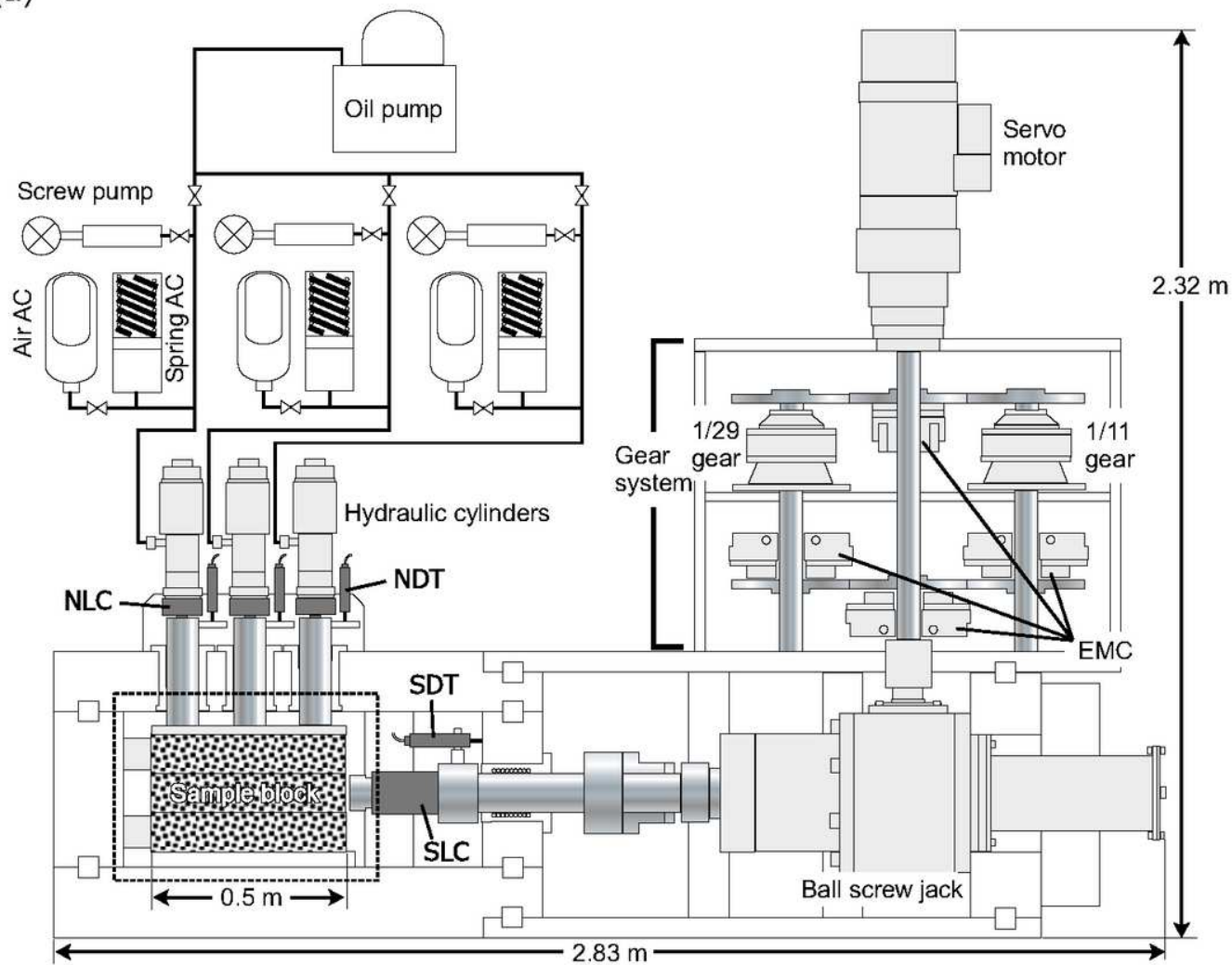


**Figure 2**

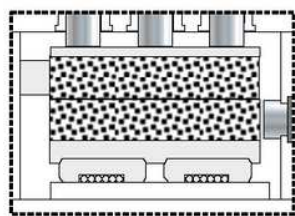
Porous tuff breccia sample used in the experiments a Photomicrograph of the tuff breccia sample under planed-polarized light. b X-ray diffraction pattern of the experimental sample. The X-ray diffraction analysis was done under the following conditions: anode is Cu, acceleration voltage is 40 kV, current is 20

mA, step size is  $0.02^\circ$ , and scan speed is  $2^\circ/\text{min}$ . Pl, plagioclase; Opx, orthopyroxene; Cpx, clinopyroxene; Sm, smectite; Hem, hematite.

(a)



(b)



(c)

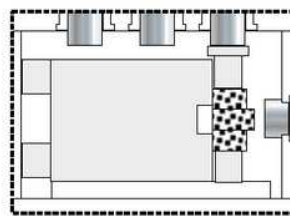


**Figure 3**

The bi-axial double direct shear loading apparatus (BASH). a Schematic diagram showing a biaxial compression apparatus built at CRIEPI, involving the sample assembly in double-direct shear configuration for a 50 cm long rock specimen. b single-direct shear sample assembly for the long specimen. c double-direct shear sample assembly for short rock specimens used in this study. The

assembly was used in this study. SLC, shear load cell; SDT, shear displacement transducer; NLC, normal load cell; NDT, normal displacement transducer; AC, accumulator; EMC, electromagnetic clutch.

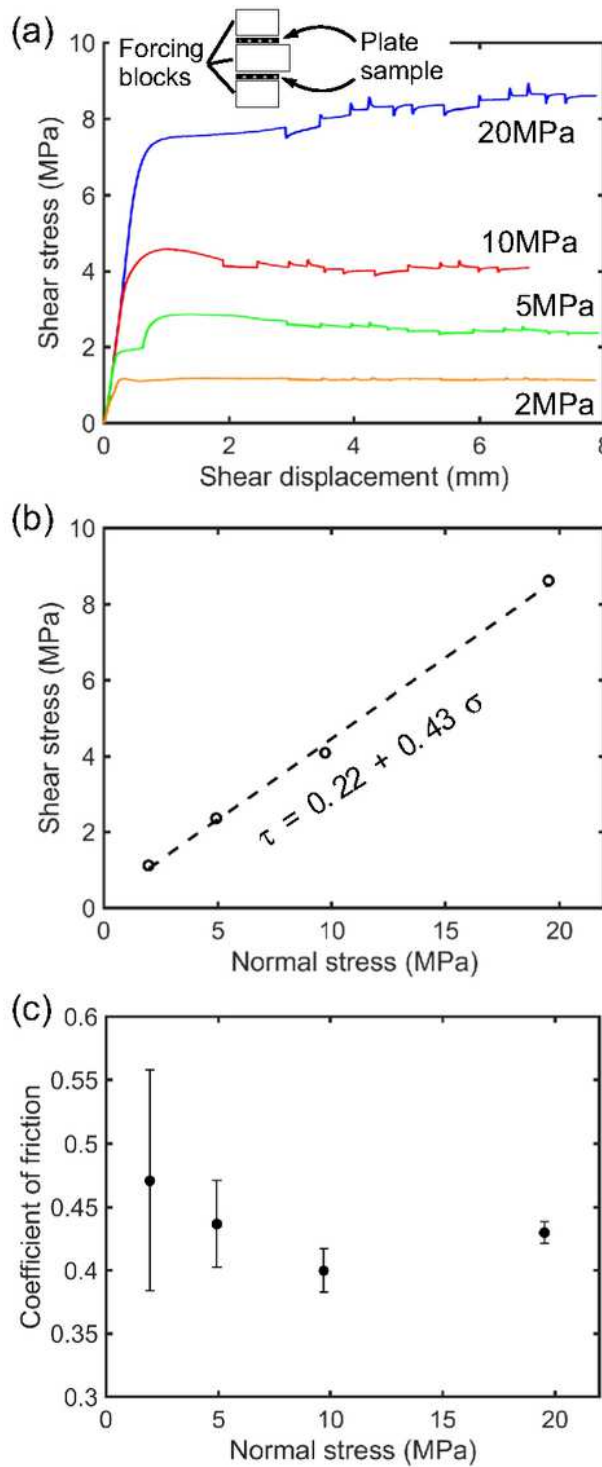


**Figure 4**

Mechanical data from velocity-stepping experiments conducted at elevated normal stress. a Shear stress versus shear displacement for the samples deformed at 2 (orange), 5 (green), 10 (red) and 20 MPa (blue). The upper left inset displays a schematic of double-direct shear configuration. b Steady state shear stress

for shear displacement > 6mm as a function of the normal stress. Friction coefficient and cohesive strength determined by a least square fit (coefficient of determination  $R^2 = 0.9975$ ) with the Mohr Coulomb linear equation (dash lines) were 0.43 ( $\pm 0.02$ ) and 0.22 ( $\pm 0.17$ ), respectively. c Steady state friction coefficient corrected for the cohesive strength (0.22 MPa) as a function of normal stress.

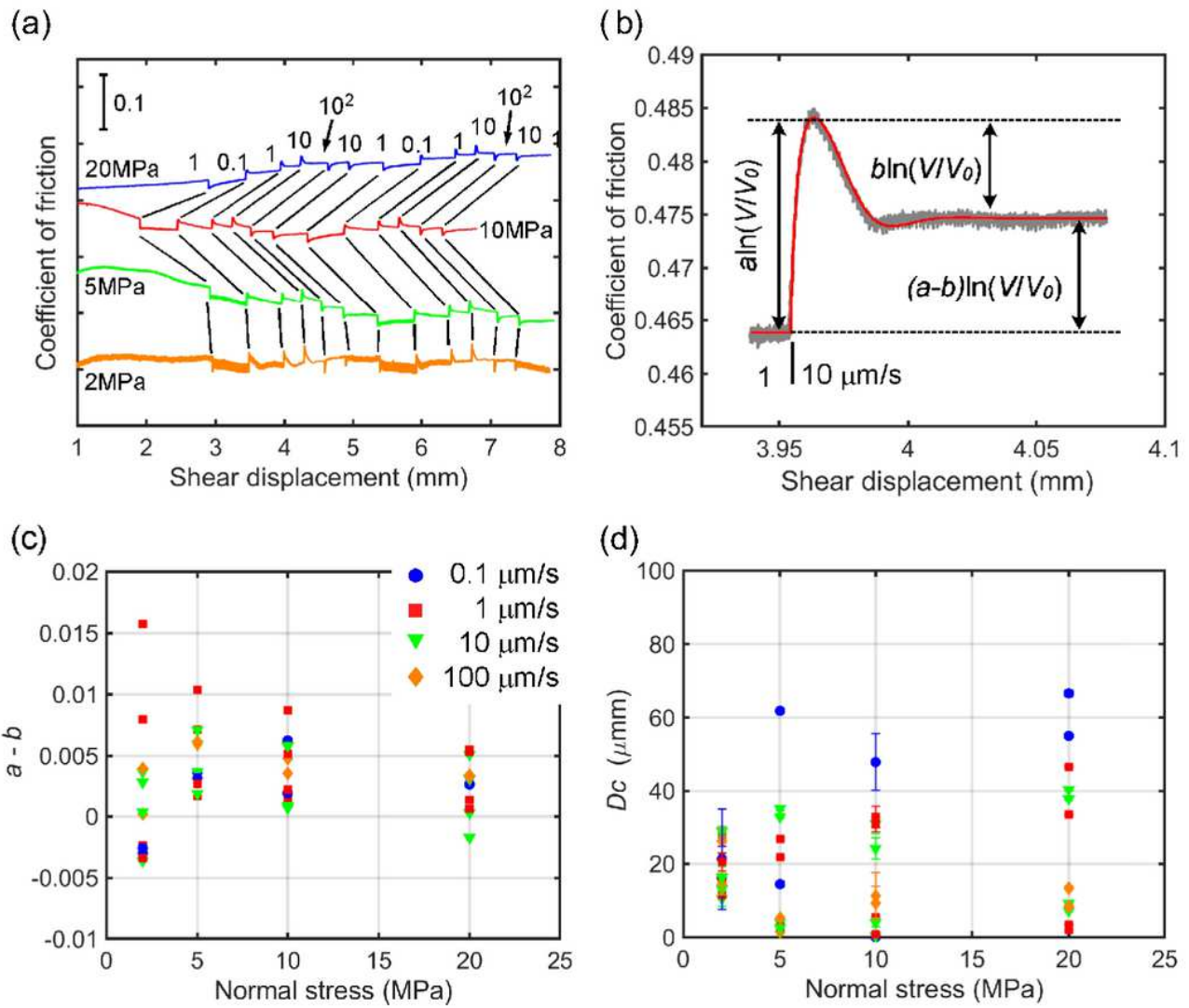


**Figure 5**

Experimental data and its friction parameter modeling results. a Friction as a function of shear displacement with velocity steps between 0.1 and 100  $\mu\text{m/s}$  at normal stresses of 2, 5, 10 and 20 MPa. Curves are offset vertically for clarity. b Example of friction response to a velocity step from 1 to 10  $\mu\text{m/s}$  (gray) with a best-fitting curve obtained from inversion analysis (red). c Velocity-dependent friction parameter ( $a - b$ ) and d critical slip distance  $D_c$  plotted as a function of normal stress for all velocity steps (blue circle, 0.1  $\mu\text{m/s}$ ; red square, 1  $\mu\text{m/s}$ ; green triangle, 10  $\mu\text{m/s}$ ; orange diamond, 100  $\mu\text{m/s}$ ).

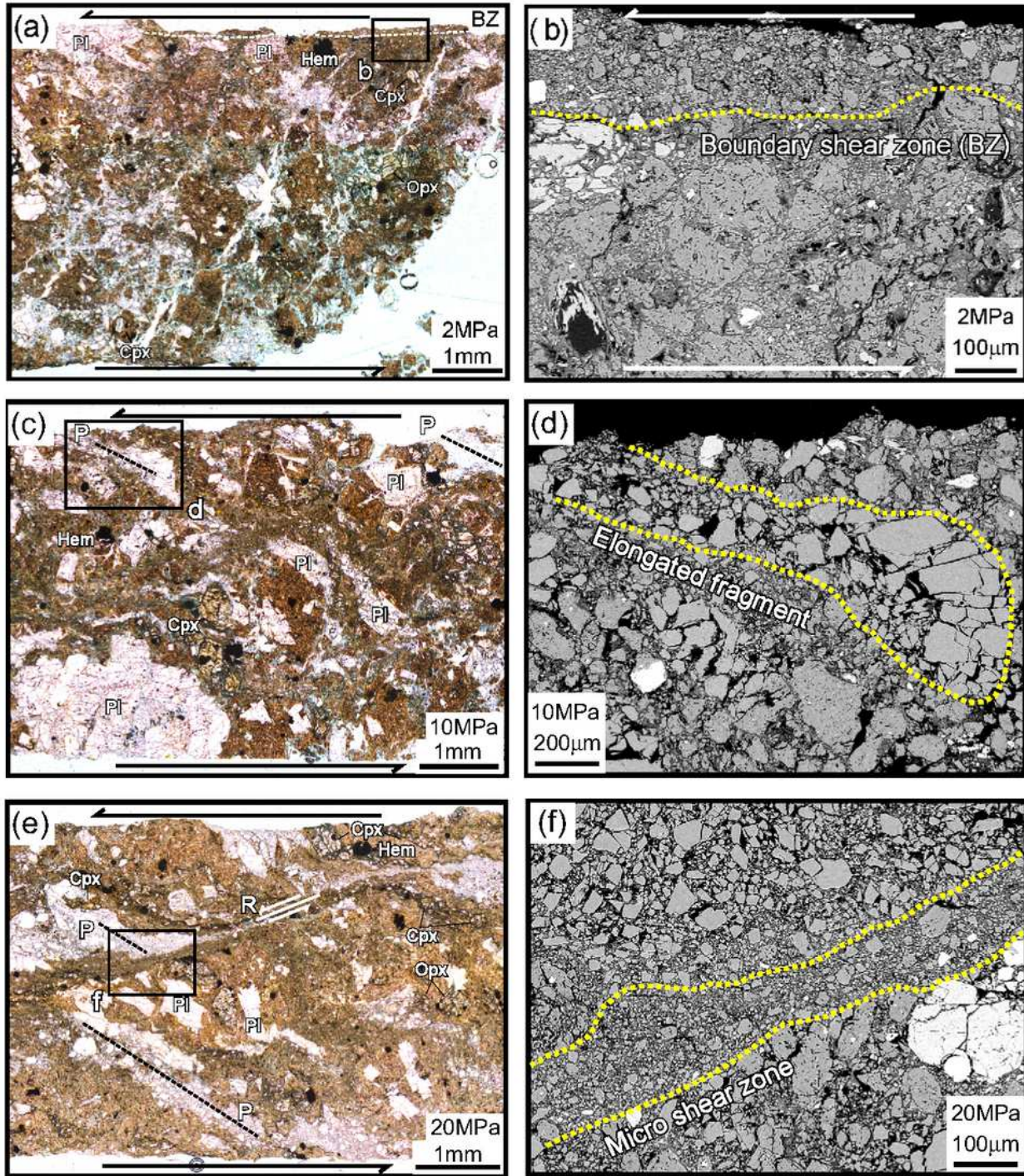


**Figure 6**

Microstructures of the deformed samples after the velocity-stepping friction tests at normal stresses of a, b 2 MPa, c, d 10 MPa and e, f 20 MPa, under optical (a, c, f) and electron (b, d, f) microscopes. Shear sense is top-to-the-left. a The boundary shear zone (BZ), of which the lower boundary is delimited by the dotted white line, is located along the upper edge of the sample. The block box gives the position of b. b A close-up view of the boundary shear zone characterized by < 20 μm small grains, located above the

dotted yellow line. c The dotted lines indicate cataclastic P foliations formed in upper part of the sample. The block box gives the position of d. d A close-up view of elongated plagioclase fragments, demarcated by the dotted yellow line, forming the cataclastic foliations. e The P foliations (dotted lines) are pervasive across the bulk sample, sometimes offset by left-lateral Riedel shears (Solid white line). The block box gives the position of f. f A close-up view of the Riedel micro shear zone bounded by the dotted yellow lines. Pl, plagioclase; Opx, orthopyroxene; Cpx, clinopyroxene; Hem, Hematite.